
PARALLEL SELECTED INVERSION FOR SPACE-TIME GAUSSIAN MARKOV RANDOM FIELDS

A PREPRINT

 **Abylay Zhumekenov**  **Elias Krainski**  **Håvard Rue**
abylay.zhumekenov@kaust.edu.sa elias.krainski@kaust.edu.sa haavard.rue@kaust.edu.sa

CEMSE Division
King Abdullah University of Science and Technology
Thuwal, 23955-6900, Saudi Arabia

September 12, 2023

ABSTRACT

Performing Bayesian inference on large spatio-temporal models requires extracting inverse elements of large sparse precision matrices for marginal variances, as well as estimating model hyperparameters. Although direct matrix factorizations can be used for the inversion, such methods fail to scale well for distributed problems when run on large computing clusters. On the contrary, Krylov subspace methods for the selected inversion have been gaining traction. We propose a parallel hybrid approach based on domain decomposition, which extends the Rao-Blackwellized Monte Carlo estimator for distributed precision matrices. Our approach exploits the strength of Krylov subspace methods as global solvers and efficiency of direct factorizations as base case solvers to compute the marginal variances and the derivatives required for hyperparameter estimation using a divide-and-conquer strategy. By introducing subdomain overlaps, one can achieve greater accuracy at an increased computational effort with little to no additional communication. We demonstrate the speed improvements and efficient hyperparameter inference on both simulated models and a massive US daily temperature data.

Keywords Latent gaussian models · spatio-temporal · selected inverse · domain decomposition · distributed

1 Introduction

A need for an efficient parallel computation of selected elements of an inverse of a large sparse precision matrix often arises, when dealing with high-dimensional Bayesian spatio-temporal models obtained from stochastic partial differential equations (SPDE) [Lindgren et al., 2011, 2022]. The SPDE-derived models are extremely useful for many applications, ranging from disease mapping to climate analysis. Coupled with the integrated nested Laplace approximation (INLA) methodology for latent Gaussian models (LGM) [Rue et al., 2009, 2017], the SPDE approach delivers the needed speed for large space-time applications. However, the growing amount of data as well as demand for high resolution modeling introduce additional computational challenges.

In particular, one of the major obstacles to a fast Bayesian inference on large LGMs is scalability of selectively inverting the posterior precision \mathbf{Q} of the latent field. The selected inverse is needed for obtaining marginal variances $\text{diag}(\mathbf{Q}^{-1})$ of the posterior latent field and for computing derivatives of the log-determinant with respect to certain hyperparameters via $\frac{\partial}{\partial \theta_j} \log |\mathbf{Q}| = \text{tr}(\mathbf{Q}^{-1} \frac{\partial}{\partial \theta_j} \mathbf{Q})$. Taking into account that the derivative evaluation is a crucial component of any gradient-based learning method, it is essential that the chosen inversion method is fast and scalable. While being sparse (see Section 2), the precision matrix could be prohibitively large for direct matrix factorizations. In this paper, we address this problem by taking a distributed hybrid approach for selected inversion.

Most conventional approaches for Bayesian inference, including INLA, rely heavily on direct matrix factorizations such as Cholesky decomposition $\mathbf{Q} = \mathbf{L}\mathbf{L}^T$ for their computations. For historical reasons, these methods were initially implemented for shared memory devices, which are constrained by memory and number of cores. There has been some recent work to parallelize INLA to run on several cluster nodes to achieve greater scalability [Fattah and Rue, 2022, Gaedke-Merzhäuser et al., 2023, 2024]. However, the implementations are limited to parallel function evaluations of the posterior, where each node stores the full precision matrix with its Cholesky factor and parallelizes matrix operations using OpenMP. The proposed methods cannot tackle larger problems, where even storing and accessing the matrix becomes challenging, let alone obtaining results in reasonable time.

The issue is handled by distributing the matrix across multiple shared memory devices or cluster nodes. Although parallel direct techniques for the inversion do exist, the scalability of such methods leaves a gap for improvement. For example, a great boost in speed is achieved for reordered 3D problems by using Takahashi equations for the selected inversion [Erisman and Tinney, 1975], instead of naively solving for the entire inverse. An additional speed can be gained by parallelizing the numerical factorization step using directed acyclic graphs (DAG) for task-scheduling [Liu, 1986]. Nevertheless, these tools are merely optimizations to an inherently serial algorithm. What prevents Cholesky to scale on large clusters is high inter-node latency and low computation-to-communication ratio of the factorization Li and Demmel [2003].

On the other hand, Krylov methods for the selected inversion have been gaining more attention recently. Krylov subspace methods is a large class of projection methods for sparse systems, which have low memory requirements, do not perform heavy matrix operations and compute only sparse matrix-vector products, which are very easy to implement and evaluate in parallel [Saad, 2003]. This allows Krylov solvers to scale extremely well in a distributed setting, and they have been extensively used for solving large problems in PDE and lately in statistics. They have also been used for large scale sampling from GMRF [Schneider and Willsky, 2003, Simpson et al., 2008, Papandreou and Yuille, 2010, Parker and Fox, 2012, Simpson et al., 2013, Chow and Saad, 2014], and more importantly, for computing certain inverse elements of large sparse matrices [Hutchinson, 1989, Tang and Saad, 2012, Sidén et al., 2018].

However, most of the papers do not go beyond shared memory implementation or do not consider the case, when it is prohibitive to store the precision matrix and its Cholesky factor on a single machine. In this paper, we will present an extension to the Rao-Blackwellized Monte Carlo algorithm from Sidén et al. [2018] for large distributed matrices for estimating hyperparameters of diffusion based spatio-temporal models [Lindgren et al., 2020]. Our method can be naturally derived using a divide-and-conquer paradigm, which connects it to many existing domain decomposition techniques. The proposed solution is fast, communication friendly, highly parallel and most importantly, distributed.

The rest of the paper is organized as follows. In Section 2, we will give a general background for existing inversion methods and Bayesian inference on non-separable spatio-temporal models. In Section 3, we demonstrate how Krylov methods can be used to compute the posterior parameters of a latent model. In particular, we will introduce a recursive algorithm for approximating the posterior marginal variance, and reformulate it as a parallel algorithm for overlapping domains. A simulation study and an application to a real world example will be given in Section 4.

2 Background

2.1 Stochastic partial differential equations approach

For the past decade, the SPDE approach has been widely used for modeling of spatio-temporal Gaussian processes [Lindgren et al., 2011][Lindgren et al., 2022]. The approach presents itself as a fast and scalable alternative to covariance matrix based methods and relies on a Gaussian Markov random field (GMRF) approximation to a continuously defined random process. The main computational advantage comes from the Markov property, which results in a sparse precision structure, allowing one to employ more efficient algorithms.

The spatial Whittle-Matérn fields serve as a starting point for constructing spatio-temporal models and many other extension of the SPDE approach. The spatial field is defined as a stationary solution $u(\mathbf{s})$ to the equation

$$\tau(\kappa^2 - \Delta)^{\alpha/2} u(\mathbf{s}) = \mathcal{W}(\mathbf{s}), \quad (1)$$

where τ is a precision parameter, κ is inversely related to the range, and α is a positive integer related to the smoothness of the field. It has been shown in Whittle [1954] and Whittle [1963] that the solution $u(\mathbf{s})$ has the Matérn covariance function. Generally, the equation could be solved using a weak formulation and a finite element discretization of the spatial domain. The approximate solution is expressed as a linear combination $\tilde{u}(\mathbf{s}) = \sum u_i \psi_i(\mathbf{s})$ of basis functions ψ_i , which are usually chosen to be piecewise linear and have a compact support. For $\alpha = 2$, one would solve for the solution \mathbf{u} the following linear system

$$\tau(\kappa^2 \mathbf{C} + \mathbf{G}) \mathbf{u} = \mathbf{z}. \quad (2)$$

Here \mathbf{C} and \mathbf{G} are sparse matrices better known as mass and stiffness matrices, respectively. Now we are interested in the precision operator of the discretized solution, let us denote it as \mathbf{Q}_s . The calculations would yield $\mathbf{Q}_s = (\kappa^2 \mathbf{C} + \mathbf{G})\mathbf{C}^{-1}(\kappa^2 \mathbf{C} + \mathbf{G})$ for $\alpha = 2$ and

$$\mathbf{Q}_s = \tau^2 \mathbf{C}^{1/2} \left(\kappa^2 \mathbf{I} + \mathbf{C}^{-1/2} \mathbf{G} \mathbf{C}^{-1/2} \right)^\alpha \mathbf{C}^{1/2}. \quad (3)$$

for the general case. It must be noted that the precision matrix is not sparse, unless the mass matrix \mathbf{C} is made diagonal. This can be done using a procedure, called ‘‘mass lumping’’, which is common in FEM applications Chen and Thomée [1985]. Then the solution vector \mathbf{u} has a distribution $\mathcal{N}(\mathbf{0}, \mathbf{Q}_s^{-1})$, where the precision matrix is sparse, and hence, \mathbf{u} is a GMRF.

2.2 Non-separable space-time models

From this point, the precision matrix in Equation (3) can be used as a building block for separable or non-separable spatio-temporal extensions. The separable case is discussed in Lindgren and Rue [2015]. A common way to construct a spatio-temporal precision matrix for a separable model is through a Kronecker product $\mathbf{Q}_u = \mathbf{Q}_t \otimes \mathbf{Q}_s$ between a temporal precision \mathbf{Q}_t and a spatial \mathbf{Q}_s derived above. However, separability is a strong assumption for most practical applications. Lindgren et al. [2020] discusses several attempts for non-separable extensions and introduces a new class of diffusion-based non-separable space-time processes.

The diffusion models can be defined by considering the spatial model first:

$$\gamma_e \mathcal{L}_s^{\alpha_e/2} v(\mathbf{s}) = \mathcal{W}(\mathbf{s}), \quad (4)$$

where $\mathcal{L}_s = \gamma_s^2 - \Delta$. The authors then construct a spatio-temporal process using the SPDE

$$\left(-\gamma_t^2 \frac{\partial^2}{\partial t^2} + \mathcal{L}_s^{\alpha_s} \right)^{\alpha_t/2} u(\mathbf{s}, t) = d\mathcal{E}(\mathbf{s}, t), \quad (5)$$

where $(\mathbf{s}, t) \in \mathcal{D} \times \mathbb{R}$, and $d\mathcal{E}(\mathbf{s}, t)$ is defined as a Gaussian noise, which is white in time, but is correlated in space according to (4). The parameters $\gamma_t, \gamma_s, \gamma_e$ are scale parameters, while $\alpha_t, \alpha_s, \alpha_e$ together determine the spatial and temporal smoothness, as well as the separability of the space-time model. The simplest non-separable case is when $(\alpha_t, \alpha_s, \alpha_e) = (1, 2, 1)$ and $d = 2$, referred to as ‘‘critical diffusion’’. The table with different parameter values and models can be found in [Lindgren et al., 2020]. These values are usually fixed to positive integers for the SPDE approach, this ensures the desired Markov property of the weights \mathbf{u} . Otherwise, rational approximations could be used for fractional values of α [Bolin and Kirchner, 2020].

The corresponding finite element approximation to the solution of (5) is expressed through the general Kronecker product basis expansion

$$u(\mathbf{s}, t) = \sum_{i=1}^{n_s} \sum_{j=1}^{n_t} u_{ij} \psi_i(\mathbf{s}) \varphi_j(t), \quad (6)$$

where ψ_i and φ_j are basis functions defined in space and time, respectively. Similar to the spatial case, piecewise linear basis functions with compact support produce a sparse system of linear equations. From there, the precision matrix of the flattened solution vector $\mathbf{u} = (u_{11}, u_{21}, \dots, u_{n_s n_t})$ can be computed as

$$\mathbf{Q}_u = \gamma_e^2 \sum_{k=0}^{2\alpha_t} \gamma_t^k \mathbf{J}(\alpha_t, k/2) \otimes \mathbf{K}(\alpha_s(\alpha_t - k/2) + \alpha_e), \quad (7)$$

for some sparse symmetric \mathbf{J} matrices coming from a temporal discretization and previously derived precision matrices \mathbf{K} of a spatial process. The variance and the range of the field are controlled jointly by hyperparameters $\gamma_t, \gamma_s, \gamma_e$, which are not interpretable when considered separately. Authors propose a reparametrization to practical spatial range, practical temporal range and marginal variance, r_s, r_t, σ^2 . A proper mapping between $\gamma_t, \gamma_s, \gamma_e$ and r_s, r_t, σ^2 for different domains and manifolds can also be found in the paper Lindgren et al. [2020].

The resulting sum of Kronecker products is sparse and inherits the block structure of corresponding temporal matrices. The in-block structure comes from the spatial mesh and can be considered arbitrary in general. While a single Kronecker product can be decomposed into a product of Cholesky factorizations, the fact that the precision matrix is expressed as a sum does not allow to reuse the factors. In general, a factorization of a sum of matrices cannot be obtained unless the matrix is assembled. On the other hand, individual factors can be used for sampling as in Papandreou and Yuille [2010]. In our case, one would need to decompose each term as

$$\begin{aligned} \mathbf{J} \otimes \mathbf{K} &= (\mathbf{L}\mathbf{L}^T) \otimes (\mathbf{R}\mathbf{R}^T) \\ &= (\mathbf{L} \otimes \mathbf{L})(\mathbf{R} \otimes \mathbf{R})^T, \end{aligned} \quad (8)$$

with \mathbf{L} , \mathbf{R} being Cholesky factors of \mathbf{J} , \mathbf{K} respectively. However, the \mathbf{J} matrices might be positive semi-definite, meaning that there is no unique Cholesky factorization and the algorithm will break down. Even if one finds such a decomposition, the proposed solution must be as robust and efficient as Cholesky for arbitrary stiffness matrices.

2.3 Latent Gaussian models

The SPDE approach is a very useful tool for setting physics informed priors for latent Gaussian models (LGM). LGM is a large class of three stage hierarchical Bayesian model that encompasses many important statistical models, including space-time diffusion models we discussed above. The three levels are observations $\mathbf{y} \in \mathbb{R}^{n_y}$, the latent Gaussian field $\mathbf{x} = (\mathbf{u}, \boldsymbol{\beta}) \in \mathbb{R}^n$ comprised of latent processes $\mathbf{u} \in \mathbb{R}^{n_u}$ and fixed effects $\boldsymbol{\beta} \in \mathbb{R}^{n_\beta}$ ($n = n_u + n_\beta$), and hyperparameters $\boldsymbol{\theta} \in \mathbb{R}^{n_\theta}$ which control the latent field and the likelihood. For the sake of simplicity and as a starting point, this paper considers the case when the likelihood is Gaussian and the hyperparameters are fixed. It is easy to generalize to unknown hyperparameters, which we will do at the end of Section 3.

$$\begin{aligned} \mathbf{y}|\mathbf{x}, \boldsymbol{\theta} &\sim \mathcal{N}(\mathbf{A}\mathbf{x}, \mathbf{Q}_y^{-1}) \\ \mathbf{x}|\boldsymbol{\theta} &\sim \mathcal{N}(\mathbf{0}, \mathbf{Q}_x^{-1}) \\ \boldsymbol{\theta} &= \boldsymbol{\theta}_0(\text{fixed}) \end{aligned} \quad (9)$$

Here, the matrix $\mathbf{A} = [\mathbf{A}_u \ \mathbf{A}_\beta] \in \mathbb{R}^{n_y \times n}$ consists of a projection matrix $\mathbf{A}_u \in \mathbb{R}^{n_y \times n_u}$ for the FEM solution (see Lindgren et al. [2011]) and $\mathbf{A}_\beta \in \mathbb{R}^{n_y \times n_\beta}$ is a thin matrix of covariates. The matrix $\mathbf{Q}_x \in \mathbb{R}^{n \times n}$ is a block diagonal prior precision matrix of \mathbf{x} , with the prior precisions $\mathbf{Q}_u \in \mathbb{R}^{n_u \times n_u}$ and $\mathbf{Q}_\beta \in \mathbb{R}^{n_\beta \times n_\beta}$ of the spatio-temporal field and the fixed effects respectively, placed on the diagonal. $\mathbf{Q}_y \in \mathbb{R}^{n_y \times n_y}$ is the precision of the observations. In general, the latent field will include other random effects as well, but we will consider a simpler setting in this paper.

The objective is to obtain the posterior marginals for the unknown latent variables \mathbf{x} . In our case, the joint posterior density corresponds to the full conditional $\pi(\mathbf{x}|\mathbf{y}) = \pi(\mathbf{x}|\mathbf{y}, \boldsymbol{\theta})$ and can be obtained analytically:

$$\mathbf{x}|\mathbf{y} \sim \mathcal{N}(\boldsymbol{\mu}, \mathbf{Q}^{-1}), \quad (10)$$

where $\mathbf{Q} = \mathbf{Q}_x + \mathbf{A}^T \mathbf{Q}_y \mathbf{A}$ is the posterior precision and $\boldsymbol{\mu} = \mathbf{Q}^{-1} \mathbf{A}^T \mathbf{Q}_y \mathbf{y}$ is the posterior mean. Then the marginal densities can be expressed as

$$x_i|\mathbf{y} \sim \mathcal{N}(\mu_i, \sigma_i^2), \quad (11)$$

where one needs to somehow compute $(\sigma_1^2, \dots, \sigma_n^2) = \text{diag}(\mathbf{Q}^{-1})$. While the mean can be computed rather easily using iterative methods, extracting diagonal elements requires selectively inverting \mathbf{Q} . We note that the selected inverse can also be used for computing $\text{tr}(\mathbf{Q}^{-1} \frac{\partial}{\partial \theta} \mathbf{Q})$ when forming the gradient. In fact, one only needs to sum over an element-wise product

$$\text{tr} \left(\mathbf{Q}^{-1} \frac{\partial}{\partial \theta} \mathbf{Q} \right) = \sum_{ij} \left(\mathbf{Q}^{-1} \right)_{ij} \left(\frac{\partial}{\partial \theta} \mathbf{Q} \right)_{ij} \quad (12)$$

between selected inverse and the matrix derivative. We will now revisit existing methods for GRMFs in more detail.

2.4 Existing methods

Most existing methods on large precision matrices rely on Krylov methods to estimate the selected entries of the inverse. Krylov subspace methods are iterative algorithms designed to efficiently solve large sparse linear systems $\mathbf{Q}\mathbf{x} = \mathbf{b}$. Given a matrix \mathbf{Q} and vector \mathbf{b} , Krylov methods approximate the solution in a subspace $\mathcal{K}_m(\mathbf{Q}, \mathbf{b}) = \text{span}\{\mathbf{b}, \mathbf{Q}\mathbf{b}, \dots, \mathbf{Q}^{m-1}\mathbf{b}\}$ of size m . These methods require only $\mathcal{O}(mn)$ storage and avoid the high computational cost of direct solvers. Their efficiency comes from simple vector operations and minimal communication, making them well-suited for large-scale problems. Additionally, their reliance on matrix-vector products makes them naturally parallelizable, further enhancing performance.

Hutchinson's stochastic estimator [Hutchinson, 1989], given in Equation (13), is one of the oldest and well known methods for estimating the diagonal of the inverse. The estimator solves a sequence of random zero-centered right hand sides $\mathbf{z}^{(k)}$ using a Krylov method, and aggregates the result by embarrassingly parallel element-wise vector operations. It is an unbiased estimator of the diagonal of the inverse and has a Monte Carlo like convergence properties, but is noisy for small sample sizes n_k .

$$\begin{aligned} \text{diag}(\mathbf{Q}^{-1}) &\approx \left[\sum_{k=1}^{n_k} \mathbf{z}^{(k)} \odot \mathbf{Q}^{-1} \mathbf{z}^{(k)} \right] \\ &\quad \odot \left[\sum_{k=1}^{n_k} \mathbf{z}^{(k)} \odot \mathbf{z}^{(k)} \right], \end{aligned} \quad (13)$$

A probing method by Tang and Saad [2012] was derived as a deterministic version of the stochastic estimator for a sparsified inverse, see Equation (14). Although the inverse is dense in general, it can be approximated by a sparse matrix with a non-zero pattern of \mathbf{Q}^{n_q} for some power n_q . In this case, one could solve for several diagonal entries simultaneously using a single right hand side $\mathbf{z}^{(k)}$ consisting of ones at corresponding entries. The idea is that if the rows of Σ decay exponentially, we can find a set of variables, which are almost independent. The authors generate the vectors $\mathbf{z}^{(k)}$ using a greedy coloring technique. The number of vectors will typically depend on the order n_q of the sparseness, which can be small for diagonally dominant matrices, but can grow large if it is not the case. For SPDE precision matrices, n_q could be somehow associated with the correlation range, meaning that n_q could be as big as n in cases where the field is extremely correlated.

$$\text{diag}(\mathbf{Q}^{-1}) \approx \text{diag}(\mathbf{Q}^{-1}\mathbf{Z}\mathbf{Z}^T) \circ \text{diag}(\mathbf{Z}\mathbf{Z}^T). \quad (14)$$

A different approach was taken by Sidén et al. [2018] and their Rao-Blackwellized Monte Carlo (RBMC) estimator. In essence, authors improve the error of a sample variance estimator by conditioning on set of neighboring elements. The marginal variances can be computed by utilizing the law of total variance. The estimator is also unbiased and has similar convergence properties, but borrows information from the precision matrix itself. The basic version is given in Equation (15), where $\mathbf{x}_{-i}^{(k)}$ denotes a sample of the latent field with its i -th element / row removed.

$$\begin{aligned} \mathbb{V}(x_i) &= \mathbb{E}[\mathbb{V}(x_i|\mathbf{x}_{-i})] + \mathbb{V}[\mathbb{E}(x_i|\mathbf{x}_{-i})] \\ &= \mathbb{E}[q_{ii}^{-1}] + \mathbb{V}[-q_{ii}^{-1}\mathbf{Q}_{i,-i}\mathbf{x}_{-i}] \\ &\approx q_{ii}^{-1} + \frac{1}{n_k} \sum_{k=1}^{n_k} q_{ii}^{-1}\mathbf{Q}_{i,-i}\mathbf{x}_{-i}^{(k)}, \end{aligned} \quad (15)$$

The authors also derive a blocked and interface versions of the algorithm. The main idea behind the interfaces is similar to creating a buffer region that absorbs effects from the conditioning set. At an increased computational cost, the estimators outperform Hutchinson’s stochastic estimator in terms of accuracy.

One of the assumptions that makes the results in Sidén et al. [2018] computationally viable is a simplified strategy for sampling from the GMRF. The precision matrix in the paper can be represented in the form $\mathbf{Q} = \mathbf{L}\mathbf{L}^T + \mathbf{R}\mathbf{R}^T$. Then, as suggested by Papandreou and Yuille [2010], one can easily sample from the posterior by solving $\mathbf{Q}\mathbf{u} = \mathbf{L}\mathbf{z} + \mathbf{R}\mathbf{w}$ using the conjugate gradient (or any Krylov) method, where \mathbf{z} and \mathbf{w} are standard Gaussian samples. However, this cannot always be done for matrices obtained from the FEM discretization of SPDE models. For instance, precision matrices for non-separable diffusion-based spatio-temporal models can be expressed as a sum of kronecker products [Lindgren et al., 2020]. However, some terms are positive semi-definite, and in such cases, the Cholesky algorithm breaks due to a zero pivot.

There are other papers that explore fast and efficient sampling of GMRFs using Krylov solvers [Schneider and Willsky, 2003, Simpson et al., 2008, Papandreou and Yuille, 2010, Parker and Fox, 2012, Simpson et al., 2013, Chow and Saad, 2014]. Most of the methods rely on Lanczos tridiagonalization of the operator \mathbf{Q} to build a low-rank approximation of the covariance matrix. However, the produced samples are of low quality and may not converge to the desired distribution. Chow and Saad [2014] proposed a better method for obtaining high quality samples by approximating $\mathbf{Q}^{-1/2}\mathbf{z}$. Although each sample is obtained using a low rank Krylov approximation, the realized covariance converges to its full rank counterpart.

In the next section, we will present our approach to solving the inversion problem with heavy emphasis on the scalability and parallel implementation. We will reformulate the results from Sidén et al. [2018] as a domain decomposition method for distributed problems and use the preconditioned Krylov sampling from Chow and Saad [2014] for parallel precision matrices.

3 Main results

3.1 Computing the mean

The posterior mean is a solution to a sparse linear system of equations

$$\boldsymbol{\mu} = \mathbf{Q}^{-1}(\mathbf{A}^T\mathbf{Q}_y\mathbf{y}). \quad (16)$$

Preconditioned Krylov methods are an efficient way to solve such systems concurrently, but the efficiency will heavily depend on the spectrum of the operator \mathbf{Q} , its sparseness and load balancing, i.e. how the system was partitioned.

Typically, large matrices are distributed according to row partitions, where each process owns only several rows of the global matrix. Then the matrix-vector products can be evaluated at each processor in parallel:

$$\mathbf{Q}\mathbf{v}^{(j)} = \begin{bmatrix} \mathbf{Q}_{\text{proc } 1} \\ \vdots \\ \mathbf{Q}_{\text{proc } p} \end{bmatrix} \mathbf{v}^{(j)} = \begin{bmatrix} \mathbf{Q}_{\text{proc } 1} \mathbf{v}^{(j)} \\ \vdots \\ \mathbf{Q}_{\text{proc } p} \mathbf{v}^{(j)} \end{bmatrix}. \quad (17)$$

However, the block structure of the posterior precision matrix \mathbf{Q} is not well suited for Krylov solvers. The structure is given below in Equation (18). The prior \mathbf{Q}_x is a block diagonal matrix consisting of a large sparse precision \mathbf{Q}_u defined through SPDE, and a small diagonal \mathbf{Q}_β corresponding to fixed effects. The matrix $\mathbf{Q}_y = \tau_y \mathbf{I}$ is a diagonal precision for observed data.

$$\begin{aligned} \mathbf{Q} &= \mathbf{Q}_x + \mathbf{A}^T \mathbf{Q}_y \mathbf{A} \\ &= \begin{bmatrix} \mathbf{Q}_u & \mathbf{0} \\ \mathbf{0} & \mathbf{Q}_\beta \end{bmatrix} + \begin{bmatrix} \mathbf{A}_u^T \\ \mathbf{A}_\beta^T \end{bmatrix} [\mathbf{Q}_y] \begin{bmatrix} \mathbf{A}_u & \mathbf{A}_\beta \end{bmatrix} \\ &= \begin{bmatrix} \mathbf{Q}_u + \mathbf{A}_u^T \mathbf{Q}_y \mathbf{A}_u & \mathbf{A}_u^T \mathbf{Q}_y \mathbf{A}_\beta \\ \mathbf{A}_\beta^T \mathbf{Q}_y \mathbf{A}_u & \mathbf{Q}_\beta + \mathbf{A}_\beta^T \mathbf{Q}_y \mathbf{A}_\beta \end{bmatrix} \\ &=: \begin{bmatrix} \mathbf{Q}_{uu} & \mathbf{Q}_{u\beta} \\ \mathbf{Q}_{\beta u} & \mathbf{Q}_{\beta\beta} \end{bmatrix} \end{aligned} \quad (18)$$

The INLA implementation uses the matrix form above for its computations, where \mathbf{A}_β , and hence $\mathbf{Q}_{\beta u}$ are dense blocks [Rue et al., 2009, 2017, Van Niekerk et al., 2023]. However, when assembling the matrix in parallel, it is important that matrix row partitions are equally sparse and balanced. The processor owning the $\mathbf{Q}_{\beta u}$ dense block will spend more time for performing more floating point operations when computing matrix-vector products $\mathbf{Q}\mathbf{v}^{(j)}$. This will result in overall algorithm slowdown, since Krylov solvers require synchronizations every or every few iterations.

Therefore, it is preferable to separate the SPDE part from the fixed effects. This can be done by conditioning on fixed effects β , which gives the conditional precision operator $\mathbf{Q}_{u|\beta} = \mathbf{Q}_{uu}$. This lets us work with a sparser and more homogeneous object \mathbf{Q}_{uu} , for which the Krylov solver will be efficient. In addition, picking a preconditioner becomes easier, as we deal with the SPDE precision only, and the covariates have no effect on the spectrum anymore. The rest is handled by appropriate dense linear algebra routines. For the equation (16), it means solving two systems

$$\begin{bmatrix} \mathbf{Q}_{uu} & \mathbf{Q}_{u\beta} \\ \mathbf{Q}_{\beta u} & \mathbf{Q}_{\beta\beta} \end{bmatrix} \begin{bmatrix} \boldsymbol{\mu}_u \\ \boldsymbol{\mu}_\beta \end{bmatrix} = \begin{bmatrix} \mathbf{A}_u^T \mathbf{Q}_y \mathbf{y} \\ \mathbf{A}_\beta^T \mathbf{Q}_y \mathbf{y} \end{bmatrix}. \quad (19)$$

By rearranging and substituting the terms, we get

$$\begin{aligned} \boldsymbol{\mu}_\beta &= \mathbf{S}^{-1} \left((\mathbf{A}_\beta^T \mathbf{Q}_y \mathbf{y}) - \mathbf{Q}_{\beta u} \mathbf{Q}_{uu}^{-1} (\mathbf{A}_u^T \mathbf{Q}_y \mathbf{y}) \right) \\ \boldsymbol{\mu}_u &= \mathbf{Q}_{uu}^{-1} \left((\mathbf{A}_u^T \mathbf{Q}_y \mathbf{y}) - \mathbf{Q}_{u\beta} \boldsymbol{\mu}_\beta \right), \end{aligned} \quad (20)$$

where $\mathbf{S} = \mathbf{Q}_{\beta\beta} - \mathbf{Q}_{\beta u} \mathbf{Q}_{uu}^{-1} \mathbf{Q}_{u\beta}$ is the Schur complement of \mathbf{Q}_{uu} in \mathbf{Q} , and also $\mathbb{V}(\beta) = \mathbf{S}^{-1}$. We note that the posterior mean requires only $n_\beta + 2$ solves with a sparse \mathbf{Q}_{uu} , one solve with a small dense \mathbf{S} , and a few additional yet cheap matrix-vector and matrix-matrix products.

3.2 Computing the variance

We can find the marginal variances by conditioning on fixed effects as

$$\begin{aligned} \text{diag}(\mathbb{V}(\mathbf{u})) &= \text{diag}(\mathbf{Q}_{uu}^{-1}) \\ &\quad + \text{diag}(\mathbf{Q}_{uu}^{-1} \mathbf{Q}_{u\beta} \mathbb{V}(\beta) \mathbf{Q}_{\beta u} \mathbf{Q}_{uu}^{-1}), \end{aligned} \quad (21)$$

where $\mathbb{V}(\beta) = \mathbf{S}^{-1}$ can be computed from the Schur complement as mentioned earlier. We see that the only additional computation is $\text{diag}(\mathbf{Q}_{uu}^{-1})$, as everything else is already computed. We will use Rao-Blackwellized Monte Carlo approach discussed in Sidén et al. [2018] to extract the diagonal of the posterior covariance $\text{diag}(\mathbb{V}(\mathbf{u}))$ in parallel. The resulting algorithm can be derived both recursively and non-recursively. We will define an algorithm on \mathbf{Q} , but we can apply the algorithm directly on \mathbf{Q} or on its submatrices, for example \mathbf{Q}_{uu} .

3.2.1 Recursive RBMC

Let us ease the notation and denote $\mathbf{x} := \mathbf{x}|y$, we will revert to the conditioning notation whenever it is necessary to be unambiguous. Then let \mathbf{x} be a GMRF with respect to an undirected graph $G = (\Omega, E)$, with sets of vertices $\Omega = \{1, \dots, n\}$ and edges $E = \{(i, j) \in \Omega \times \Omega : x_i \perp x_j | x_{-ij}\}$, similar to the definition in Rue and Held [2005]. A separating set S is a set of vertices that disconnects the graph into two disjoint subgraphs with vertices Ω_1 and Ω_2 . That is, there exists no $(i, j) \in \Omega_1 \times \Omega_2$ such that $(i, j) \in E$. In probabilistic terms, \mathbf{x}_{Ω_1} and \mathbf{x}_{Ω_2} are conditionally independent, given \mathbf{x}_S .

Now, let $\mathbf{Q}_{\Omega_1\Omega_1}$ and $\mathbf{Q}_{\Omega_2\Omega_2}$ be principal submatrices obtained by selecting rows and columns indexed by Ω_1 and Ω_2 , respectively. We form $\mathbf{Q}_{\Omega_1 S}$, $\mathbf{Q}_{\Omega_2 S}$ and \mathbf{x}_S in a similar fashion. Using the law of total variance, we obtain

$$\begin{aligned} \mathbb{V}(\mathbf{x}_{\Omega_1}) &= \mathbb{E}(\mathbb{V}(\mathbf{x}_{\Omega_1} | \mathbf{x}_S)) + \mathbb{V}(\mathbb{E}(\mathbf{x}_{\Omega_1} | \mathbf{x}_S)) \\ &= \mathbf{Q}_{\Omega_1\Omega_1}^{-1} + \mathbb{V}(\mathbf{Q}_{\Omega_1\Omega_1}^{-1} \mathbf{Q}_{\Omega_1 S} \mathbf{x}_S) \end{aligned} \quad (22)$$

and

$$\mathbb{V}(\mathbf{x}_{\Omega_2}) = \mathbf{Q}_{\Omega_2\Omega_2}^{-1} + \mathbb{V}(\mathbf{Q}_{\Omega_2\Omega_2}^{-1} \mathbf{Q}_{\Omega_2 S} \mathbf{x}_S) \quad (23)$$

for the other half. We can see that the only common term in formulas (22) and (23) is \mathbf{x}_S . That is, we can compute these two separately and in parallel, given samples of \mathbf{x}_S to evaluate the variance term.

Moreover, computing the first term $\mathbf{Q}_{\Omega_1\Omega_1}^{-1}$ or $\mathbf{Q}_{\Omega_2\Omega_2}^{-1}$ is exactly the same problem as computing \mathbf{Q}^{-1} , but half the size. We could repeat the procedure for $\mathbf{x}_{\Omega_1} | \mathbf{x}_S$ to produce a partition $\Omega_{11}, \Omega_{12}, S_1$, subsets $\mathbf{x}_{\Omega_{11}}, \mathbf{x}_{\Omega_{12}}$ and a conditioning set $\mathbf{x}_{S \cup S_1}$. We could keep splitting until we reach a dimension small enough for direct methods. This allows a recursive specification of the inversion problem, a sketch of the algorithm is given in Algorithm 3.1, as well as an illustration of the divide-and-conquer strategy in Figure 1.

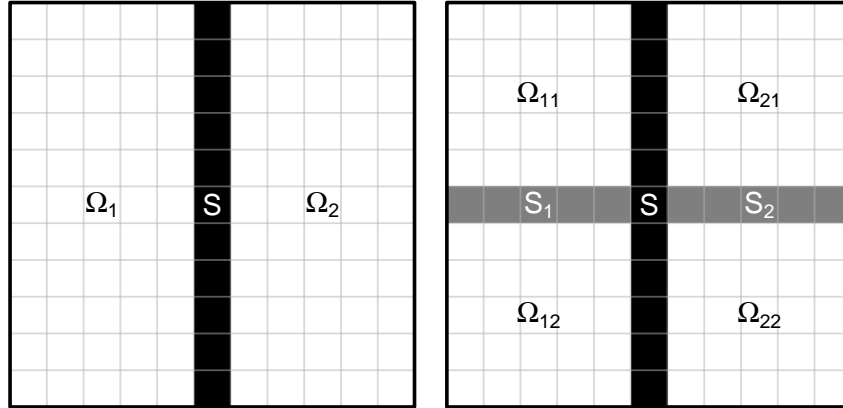


Figure 1: Two iterations of the recursive dissection algorithm

The algorithm computes the diagonal blocks of the covariance matrix using a divide-and-conquer tactics. It can be further simplified to compute only the diagonal entries. The only costly computations here are inverting a matrix \mathbf{Q} at the bottom of the recursion and evaluating $\mathbf{Q}_{\Omega_1\Omega_1}^{-1} \mathbf{Q}_{\Omega_1 S} \mathbf{x}_S$ and $\mathbf{Q}_{\Omega_2\Omega_2}^{-1} \mathbf{Q}_{\Omega_2 S} \mathbf{x}_S$. The base case inversion can be done efficiently using a direct solver, whereas Krylov methods can be used to solve linear systems with $\mathbf{Q}_{\Omega_1\Omega_1}$ and $\mathbf{Q}_{\Omega_2\Omega_2}$.

3.2.2 Parallel RBMC

Although conceptually simple, the recursive implementation would be inefficient and hard to implement. Setting up a preconditioned Krylov solver for each $\mathbf{Q}_{\Omega_1\Omega_1}$ at each level would have a huge overhead. In addition, a thorough bookkeeping would be needed for complicated ownership patterns of the original matrix \mathbf{Q} by different processes. Ideally, each subproblem inherits a processor from the parent problem, but it is unclear how the separators should be distributed.

A better approach would be to flatten out the recursion, and tackle the problem from the domain decomposition point of view. Consider partitioning the graph of \mathbf{Q} into n_p parts using nested dissection. Denote Ω_p to be the partitions and S to be a union of vertex separators. The same partitioning is obtained at leaf nodes if we naively apply the recursive

Algorithm 3.1 Recursive RBMC

Input: $\mathbf{Q}, \mathbf{x}_{S_0}$
if \mathbf{Q} is small **then**
 return \mathbf{Q}^{-1}
end if
 $\Sigma = \mathbf{0}$
Partition the graph into Ω_1, Ω_2, S
Set $S := S \cup S_0$
 $\Sigma_{\Omega_1\Omega_1} = \text{RBMC}(\mathbf{Q}_{\Omega_1\Omega_1}, \mathbf{x}_S)$
 $+ \mathbb{V}(\mathbf{Q}_{\Omega_1\Omega_1}^{-1} \mathbf{Q}_{\Omega_1 S} \mathbf{x}_S)$
 $\Sigma_{\Omega_2\Omega_2} = \text{RBMC}(\mathbf{Q}_{\Omega_2\Omega_2}, \mathbf{x}_S)$
 $+ \mathbb{V}(\mathbf{Q}_{\Omega_2\Omega_2}^{-1} \mathbf{Q}_{\Omega_2 S} \mathbf{x}_S)$
 $\Sigma_{SS} = \mathbb{V}(\mathbf{x}_S)$
Return Σ

Output: Σ

RBMC algorithm. Important part is that given \mathbf{x}_S , all of \mathbf{x}_{Ω_p} are conditionally independent from each other. Then we can rewrite the algorithm in a more parallel friendly way.

Algorithm 3.2 Parallel RBMC

Input: \mathbf{Q}
 $\Sigma = \mathbf{0}$
Partition the graph into non-overlapping Ω_p , separated by S
for $p = 1, \dots, n_p$ **in parallel do**
 $\Sigma_{\Omega_p\Omega_p} = \mathbf{Q}_{\Omega_p\Omega_p}^{-1} + \mathbb{V}(\mathbf{Q}_{\Omega_p\Omega_p}^{-1} \mathbf{Q}_{\Omega_p S} \mathbf{x}_S)$
end for
 $\Sigma_{SS} = \mathbb{V}(\mathbf{x}_S)$
Return Σ

Output: Σ

The one crucial difference of this variant from the recursive is that the partitioning of the graph is done only once. This helps to distribute the problem more efficiently and avoid unnecessary movement of data. In addition, each subproblem has exactly one operator $\mathbf{Q}_{\Omega_p\Omega_p}$, which is factored for the direct solution $\mathbf{Q}_{\Omega_p\Omega_p}^{-1}$ and can be reused when computing the variance of $\mathbf{Q}_{\Omega_p\Omega_p}^{-1} \mathbf{Q}_{\Omega_p S} \mathbf{x}_S$.

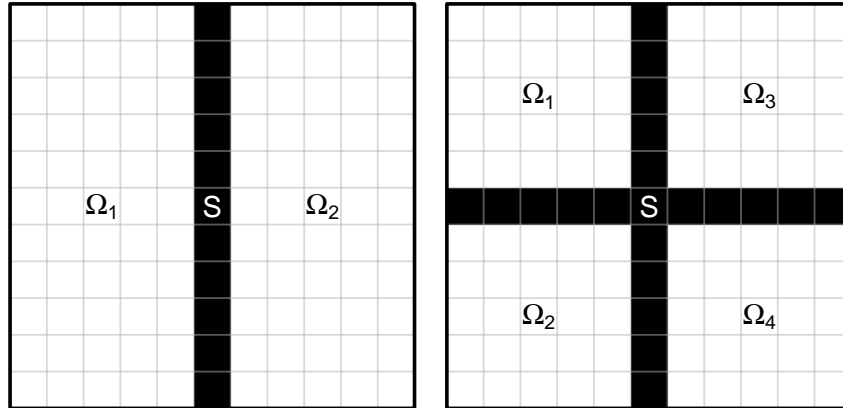


Figure 2: Schur's complement method for 2 and 4 subdomains

The algorithm is a stochastic version of the iterative substructuring, also called the Schur complement method. The substructuring method computes $\mathbb{V}(\mathbf{x}_S)$ as an inverse of the Schur complement

$$\Sigma_{SS} = \left(\mathbf{Q}_{SS} - \sum_{p=1}^{n_p} \mathbf{Q}_{S\Omega_p} \mathbf{Q}_{\Omega_p\Omega_p}^{-1} \mathbf{Q}_{\Omega_p S} \right)^{-1}. \quad (24)$$

As we see, the Schur complement itself can be computed and assembled in parallel, by solving with $\mathbf{Q}_{\Omega_p\Omega_p}$. However, the Schur complement is a dense $|S| \times |S|$ matrix in general, and the dimensions of the separator is $\mathcal{O}(n^{2/3})$ for 3D problems. For large scale problems, this method can quickly become prohibitive. We avoid such bottlenecks, at a cost of accuracy, by approximating the variance using samples from \mathbf{x}_S .

3.2.3 Overlapping RBMC

Approximating the variance term in Algorithm 3.2 via sampling introduces a Monte Carlo error. The uncertainty in \mathbf{x}_S propagates to the rest of the partition Ω_p as well. The error can be decreased by increasing the number of samples of \mathbf{x}_S . Alternatively, it can also be reduced by pushing the separator outwards, which was also done in Sidén et al. [2018]. Doing this lessens the dependency of the interior parts of Ω_p from S , since the correlation has to travel further. The similar idea has been used to absorb the effects from the boundary for the SPDE approach on compact domains [Lindgren et al., 2011].

The idea can be better explained on a simpler one-dimensional example. Consider a stationary auto-regressive AR(1) process $x_i = \phi x_{i-1} + \epsilon_i$ for $i = 1, \dots, 99$ with $\phi = 0.95$. Let $\mathbf{x}_{\Omega_1} = (x_1, \dots, x_{49})$, $\mathbf{x}_{\Omega_2} = (x_{51}, \dots, x_{99})$ and $\mathbf{x}_S = (x_{50})$ be disjoint partitions obtained in Algorithm 3.2. Now we define two overlapping partitions $\mathbf{x}_{\Omega_1^*} = (x_1, \dots, x_{59})$ and $\mathbf{x}_{\Omega_2^*} = (x_{41}, \dots, x_{99})$, created by extending the partitions by $n_l = 10$ lags. The corresponding separators are $\mathbf{x}_{S_1} = (x_{60})$ and $\mathbf{x}_{S_2} = (x_{40})$. For both partitioning schemes we can compute the RBMC estimates of marginal variances and the relative root mean square errors (RMSE). The RMSE of MC and RBMC estimators are $\sqrt{2/n_k}$ and $\phi^{2n_l} \sqrt{2/n_k}$, for a sample size n_k and a distance n_l from the separator.

First, we plot the error for non-overlapping partitions on the left of Figure 3. We can clearly see the error decaying as we move away from the separating set, with the highest error being equal to the MC error exactly at the separator. Then we shift the respective separators by 10 lags in opposite directions and get the second graph in Figure 3. Here we restrict the variance estimates to match the original partitioning scheme, and discard the values that were on intervals overlapping with the exterior (dashed lines). We will call this estimator the overlapping RBMC. A two-dimensional example is shown in Figure 4.

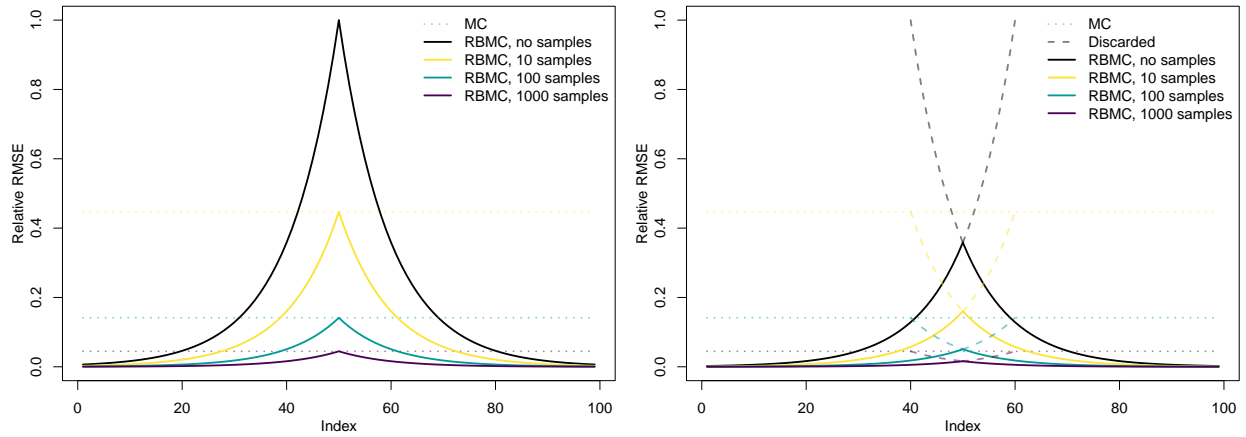


Figure 3: Relative RMSE of parallel (left) and overlapping (right) RBMC estimators with various sample sizes for an AR-1 model with $\phi = 0.95$.

A good choice of n_l would be the lag, at which correlation drops to zero. For discretely indexed temporal 1D problems it is the temporal correlation r_t , for spatial 2D problems on a discrete grid it is the spatial correlation r_s . For spatio-temporal 3D models on a continuous domain, it is more complicated. The spatial correlation will not decrease by the same amount as the temporal correlation for the same graph distance. A better strategy would be to have separate

overlap parameters $n_{l,s}$ and $n_{l,t}$ based on graph distance at which $r_s \approx 0$ and $r_t \approx 0$. Although two range parameters interact when the field is non-separable, the actual temporal range is usually smaller than r_t . In addition, the posterior range tends to be smaller than the prior, as the data introduces some degree of diagonal dominance to the precision matrix. This leads to unnecessarily larger partitions, but makes the overlap construction somewhat robust, since we always cover the high correlation regions.

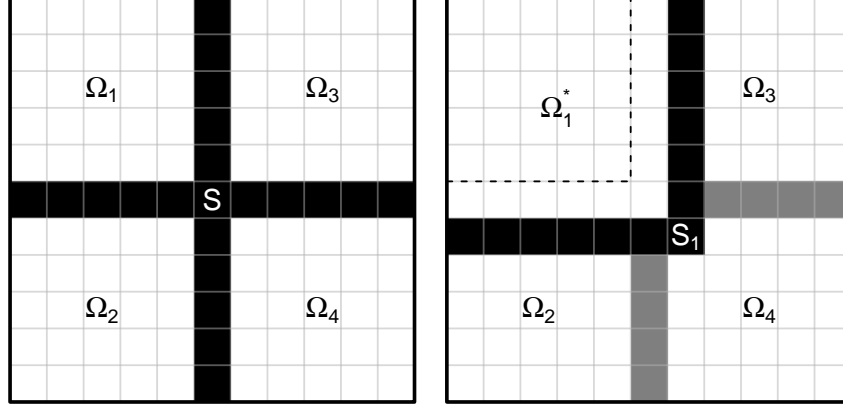


Figure 4: Initial partitioning and the extended subdomain Ω_1^* ($n_l = 1$) with its separating set S_1 .

Now we present an overlapping version of the RBMC estimator in Algorithm 3.3. For the sake of simplicity, the algorithm has only one overlap parameter n_l . First, denote $N(\Omega_p)$ to be the indices of graph neighbors of \mathbf{x}_{Ω_p} , i.e. the nodes at an exact distance 1. Then we can generate the overlapping regions Ω_p^* by extending the original partitions Ω_p to its neighbor nodes at a distance n_l . The separating sets S_p are $(n_l + 1)$ -th order neighbors, computed in a similar fashion. Then we proceed with computing marginal variances for overlapping partitions Ω_p^* . At the end of the algorithm, we apply a diagonal partition of unity operator \mathbf{P}_p , which selects rows of $\Sigma_{\Omega_p^* \Omega_p^*}$ corresponding to indices of non-overlapping Ω_p . The two-dimensional example of such extensions and overlaps is illustrated in Figure 4, where we partition a square region into 4 parts and compute separator for each of them.

Algorithm 3.3 Overlapping RBMC

Input: \mathbf{Q}

Partition the graph into non-overlapping Ω_p

for $p = 1, \dots, n_p$ **in parallel do**

Set $\Omega_p^* = \Omega_p$ and $S_p = N(\Omega_p) \setminus \Omega_p$

for $l = 1, \dots, n_l$ **do**

$\Omega_p^* = \Omega_p^* \cup S_p$

$S_p = N(\Omega_p^*) \setminus \Omega_p^*$

end for

$\Sigma_{\Omega_p \Omega_p^*} = \mathbf{P}_p \left(\mathbf{Q}_{\Omega_p^* \Omega_p^*}^{-1} + \mathbb{V}(\mathbf{Q}_{\Omega_p^* \Omega_p^*}^{-1} \mathbf{Q}_{\Omega_p^* S_p} \mathbf{x}_{S_p}) \right)$

end for

Return Σ

Output: Σ

We can get a simplified version of the algorithm for the diagonal elements only, which is given in 3.4. As we see in Algorithm 3.4, the main bulk of computations inside an outer loop is done in parallel. The algorithm consists of three main phases: computing the extension and a separator, a direct factorization, and a sampling and correction phase. Graph partitioning can be done efficiently using either the nested dissection algorithm or the multilevel partitioning techniques, both of which are implemented in METIS/ParMETIS library. Computing the neighbor nodes from the adjacency list is very straightforward, and can be done in parallel, if each processor stores the full list. Otherwise, some communication must be done to retrieve such information. For the direct solution $\text{diag}(\mathbf{Q}_{\Omega_p^* \Omega_p^*}^{-1})$, a highly efficient selected inversion algorithm [Verbosio et al., 2017] can be used. Selected inversion scales with the number of nonzeros in $\mathbf{Q}_{\Omega_p^* \Omega_p^*}$ and has already been implemented in the PARDISO and MUMPS solvers. The factorization from this phase

can then be reused for computing the correction in the sampling phase. Since we only need the diagonal of the sample variance, computations may be expressed in terms of elementwise products \odot . The samples can be generated using a Krylov solver, which we will discuss soon.

Algorithm 3.4 Overlapping RBMC for diagonal elements

Input: \mathbf{Q}

 Partition the graph into non-overlapping Ω_p
for $p = 1, \dots, n_p$ **in parallel do**

 Set $\Omega_p^* = \Omega_p$ and $S_p = N(\Omega_p) \setminus \Omega_p$
for $l = 1, \dots, n_l$ **do**
 $\Omega_p^* = \Omega_p^* \cup S_p$
 $S_p = N(\Omega_p^*) \setminus \Omega_p^*$
end for
 $\text{diag}(\Sigma_{\Omega_p^* \Omega_p^*}) = \text{diag}(\mathbf{Q}_{\Omega_p^* \Omega_p^*}^{-1})$
for $k = 1, \dots, n_k$ **do**

 Sample $\mathbf{x}^{(k)}$ using a Krylov solver

 $\text{diag}(\Sigma_{\Omega_p^* \Omega_p^*}) = \text{diag}(\Sigma_{\Omega_p^* \Omega_p^*})$

$$+ \frac{1}{n_k} \left(\mathbf{Q}_{\Omega_p^* \Omega_p^*}^{-1} \mathbf{Q}_{\Omega_p^* S_p} \mathbf{x}_{S_p}^{(k)} \right)$$

$$\odot \left(\mathbf{Q}_{\Omega_p^* \Omega_p^*}^{-1} \mathbf{Q}_{\Omega_p^* S_p} \mathbf{x}_{S_p}^{(k)} \right)$$

end for
 $\text{diag}(\Sigma_{\Omega_p \Omega_p}) = \mathbf{P}_p \text{diag}(\Sigma_{\Omega_p^* \Omega_p^*})$
end for

 Return $\text{diag}(\Sigma)$
Output: $\text{diag}(\Sigma)$

3.3 Sampling

We note that the algorithm requires one to be able to sample from the separating set \mathbf{x}_G . In Sidén et al. [2018], authors can represent the posterior precision in the form $\mathbf{Q} = \mathbf{L}\mathbf{L}^T + \mathbf{R}\mathbf{R}^T$ for some factors \mathbf{L} and \mathbf{R} . Then, as suggested by Papandreou and Yuille [2010], one can easily sample from the posterior by solving $\mathbf{Q}\mathbf{x} = \mathbf{L}\mathbf{z} + \mathbf{R}\mathbf{w}$ using the conjugate gradient, where \mathbf{z} and \mathbf{w} are standard Gaussian samples. However, this cannot be done for diffusion based models as was discussed in Section 2. Instead, we will use the Lanczos quadrature to evaluate the inverse square root of the precision operator $\mathbf{Q}^{-1/2}\mathbf{x}$.

3.3.1 Lanczos quadrature for matrix functions

The Lanczos process lays in the heart of Krylov methods for symmetric matrices. The process generates the Krylov subspace $\mathcal{K}_m(\mathbf{Q}, \mathbf{v}^{(0)})$ by evaluating matrix vector products $\mathbf{Q}\mathbf{v}^{(j)}$ and orthogonalizing them against previously computed vectors. So far, we have used the Krylov solvers as a polynomial approximation to the true solution $\mathbf{Q}^{-1}\mathbf{z} \approx q(\mathbf{Q})\mathbf{z}$. The same can be done for approximating matrix functions $f(\mathbf{Q})\mathbf{z}$, by projecting $f(\mathbf{Q})\mathbf{z}$ onto the Krylov subspace. The approximation is optimal 2-norm sense [Chow and Saad, 2014] and is

$$f(\mathbf{Q})\mathbf{z} \approx \mathbf{V}f(\mathbf{T})(\eta\mathbf{e}_1), \quad (25)$$

where \mathbf{V} are orthogonalized Krylov vectors starting with $\mathbf{v}^{(0)} = \mathbf{z}/\eta$, $\eta = \|\mathbf{z}\|$, \mathbf{T} is a small tridiagonal matrix of Lanczos coefficients and \mathbf{e}_1 is the first column of an $m \times m$ identity matrix.

The above is also nicely connected to approximating the Riemann-Stieltjes integral representation of the quadratic form

$$\begin{aligned} \mathbf{z}^T f(\mathbf{Q})\mathbf{z} &= \mathbf{z}^T \mathbf{\Upsilon} f(\mathbf{\Lambda}) \mathbf{\Upsilon}^T \mathbf{z} \\ &= \sum_{i=1}^n f(\lambda_i) \omega_i^2 \\ &= \int f(t) d\omega(t), \end{aligned} \quad (26)$$

where $\mathbf{Q} = \mathbf{\Upsilon}\mathbf{\Lambda}\mathbf{\Upsilon}^T$ is the eigendecomposition, $w_i = (\mathbf{\Upsilon}^T \mathbf{z})_i$, and $\omega(t)$ is a piece-wise constant measure representing the distribution of ω_i^2/η^2 [Golub and Meurant, 1994][Ubaru et al., 2017]. Then, the link can be established by approximating the integral with Gauss quadrature

$$\int f(t)d\omega(t) \approx \sum_{j=1}^m (\eta \tilde{v}_{1j})^2 f(\tilde{\lambda}_j), \quad (27)$$

where the nodes and weights can be elegantly obtained from the Lanczos process [Golub and Meurant, 1994]. Here, $\tilde{\lambda}_j$ is the j -th eigenvalue of the Lanczos' tridiagonal matrix \mathbf{T} , and \tilde{v}_{1j} is the first entry of the corresponding eigenvector. By denoting $\mathbf{T} = \tilde{\mathbf{Y}}\tilde{\mathbf{\Lambda}}\tilde{\mathbf{Y}}^T$, we can reassemble the approximation above as

$$\begin{aligned} \mathbf{z}^T f(\mathbf{Q})\mathbf{z} &\approx \sum_{j=1}^m (\eta \tilde{v}_{1j})^2 f(\tilde{\lambda}_j) \\ &= (\eta \mathbf{e}_1)^T \tilde{\mathbf{Y}} f(\tilde{\mathbf{\Lambda}}) \tilde{\mathbf{Y}}^T (\eta \mathbf{e}_1) \\ &= (\eta \mathbf{e}_1)^T f(\tilde{\mathbf{Y}}\tilde{\mathbf{\Lambda}}\tilde{\mathbf{Y}}^T) (\eta \mathbf{e}_1) \\ &= \mathbf{z}^T \mathbf{V} f(\mathbf{T}) (\eta \mathbf{e}_1), \end{aligned} \quad (28)$$

which we can recognize as a product between \mathbf{z}^T and the approximation to $f(\mathbf{Q})\mathbf{z}$.

3.3.2 Preconditioned Krylov sampling

We could use the formula in Equation (25) to sample from a posterior GMRF by taking \mathbf{Q} as our operator, \mathbf{z} as the right hand side, and $f(z) = z^{-1/2}$ as our function. As long as the dimension of the Krylov subspace stays low, it is rather easy to compute $f(\mathbf{T}) = \mathbf{T}^{-1/2}$ through the eigendecomposition to find weights for \mathbf{V} . On the contrary, if the condition number of \mathbf{Q} is large, it results in longer iterations and higher memory requirements. Therefore, preconditioning is a crucial step to keep the algorithm efficient. However, the sampling formula in Equation (25) becomes more complicated, and will depend on the type of preconditioner we will use. We will further follow the results of Chow and Saad [2014].

We consider a symmetric split preconditioning obtained from incomplete factorization of \mathbf{Q} . For example, an incomplete Cholesky with zero fill-in IC(0) [Saad, 2003], or its block version called block Jacobi. The preconditioned operator then becomes $\tilde{\mathbf{Q}} = \mathbf{L}^{-1}\mathbf{Q}\mathbf{L}^{-T}$, and we can evaluate an inverse square root by building the subspace $\mathcal{K}_m(\tilde{\mathbf{Q}}, \mathbf{z})$,

$$\tilde{\mathbf{x}} = \tilde{\mathbf{Q}}^{-1/2} \mathbf{z} \approx \mathbf{V}\mathbf{T}^{-1/2}(\eta \mathbf{e}_1). \quad (29)$$

The vector $\tilde{\mathbf{x}}$ has an approximate covariance

$$\tilde{\mathbf{Q}}^{-1} = (\mathbf{L}^{-1}\mathbf{Q}\mathbf{L}^{-T})^{-1} = \mathbf{L}^T \mathbf{Q}^{-1} \mathbf{L}, \quad (30)$$

that is, $\tilde{\mathbf{x}} \sim \mathcal{N}(\mathbf{0}, \mathbf{L}^T \mathbf{Q}^{-1} \mathbf{L})$. To rewind the effect of the preconditioner, we only need to be able to apply \mathbf{L}^{-T} . Then

$$\mathbf{x} = \mathbf{L}^{-T} \tilde{\mathbf{x}} \approx \mathbf{L}^{-T} \mathbf{V}\mathbf{T}^{-1/2}(\eta \mathbf{e}_1) \quad (31)$$

has an approximately Gaussian density $\mathbf{x} \sim \mathcal{N}(\mathbf{0}, \mathbf{Q}^{-1})$. The Algorithm 3.5 below generates K samples for \mathbf{x} , from which we can select the desired elements \mathbf{x}_{S_p} for our overlapping RBMC estimator in Algorithm 3.3.

Several practical consideration must be taken into account when implementing the sampler. First, we must solve a system for each new $\mathbf{z}^{(k)}$. Reusing the same subspace for different samples will produce lower quality samples. Such an approach corresponds to sampling from a low-rank approximation $\tilde{\mathbf{Q}}^{-1} \approx \mathbf{V}\mathbf{T}^{-1}\mathbf{V}^T$, which is very inaccurate unless m is close to n . For multiple right hand sides, we must generate the subspace and perform eigendecomposition each time we solve a system. Although the cost is higher, the quality of samples will be much better.

Second, the preconditioned right hand side must be $\mathbf{z}^{(k)}$, meaning that the original unpreconditioned problem we must solve is $\mathbf{Q}\mathbf{x} = \mathbf{L}\mathbf{z}^{(k)}$. Therefore, when using Krylov solvers, one must premultiply the right hand side by an incomplete factor \mathbf{L} before an actual solve. However, Krylov solvers (such as PETSc) provide implementations only for applying \mathbf{L}^{-1} or \mathbf{L}^{-T} , but never \mathbf{L} . In such cases, one might need to customize the solver or the preconditioner, to pass \mathbf{z} directly as a preconditioned right hand side.

Third, the eigendecomposition of $\mathbf{T}^{-1/2}$ cannot be replaced by a solve with a Cholesky factor. Although both options are valid inverse square root operators, our approximation implicitly relies on quadrature nodes and weights obtained from

Algorithm 3.5 Preconditioned Krylov sampler**Input:** \mathbf{Q} Compute a factored symmetric preconditioner $\mathbf{L}\mathbf{L}^T \approx \mathbf{Q}$ **for** $k = 1, \dots, n_k$ **do**Generate $\mathbf{z}^{(k)} \sim \mathcal{N}(\mathbf{0}, \mathbf{I})$ Construct $\mathcal{K}(\tilde{\mathbf{Q}}, \mathbf{z}^{(k)})$ and obtain \mathbf{T}, \mathbf{V} using preconditioned MINRES/GMRESEigendecomposition $\mathbf{T} = \tilde{\mathbf{U}}\tilde{\mathbf{\Lambda}}\tilde{\mathbf{U}}^T$ Compute $\tilde{\mathbf{x}} = \mathbf{V}\tilde{\mathbf{Y}}\tilde{\mathbf{\Lambda}}^{-1/2}\tilde{\mathbf{Y}}^T(\eta\mathbf{e}_1)$ Rewind the preconditioner $\mathbf{x}^{(k)} = \mathbf{L}^{-T}\tilde{\mathbf{x}}$ **end for****Output:** $\{\mathbf{u}_1, \dots, \mathbf{u}_{n_k}\}$

the eigendecomposition of \mathbf{T} . In practice, the decomposition is performed by each processor instead of parallelizing it. This saves communication cost and the computational overhead is not big. The structure of \mathbf{T} becomes very convenient, since we do not have to tridiagonalize the matrix \mathbf{T} for an eigendecomposition, and instead we can call optimized LAPACK routines directly.

Fourth, there are no natural tools to measure closeness of matrix function approximations when using Krylov solvers. Some analysis has been done for decaying matrix functions [Frommer et al., 2021]. However, in practice, the residuals of a solution $\mathbf{Q}^{-1}\mathbf{z}$ are used as a criterion, despite $f(\mathbf{Q})\mathbf{z}$ converging differently in general.

3.4 Hyperparameter estimation

Now assume the hyperparameters are unknown and we want the mode of the marginal density $\pi(\boldsymbol{\theta}|\mathbf{y})$. First, we impose a prior $\pi(\boldsymbol{\theta})$ on hyperparameters of the LGM model. One can use penalizing complexity (PC) priors Simpson et al. [2017] on the precision of the likelihood τ_y , log-range $\log r_s$, log r_t and log-variance σ^2 of the spatio-temporal field (see Lindgren et al. [2020]). Then the marginals of the hyperparameters can be computed as a ratio of the joint and the full conditional, which is exact in Gaussian likelihood case and is called Laplace approximation for other likelihoods Rue et al. [2009, 2017].

$$\pi(\boldsymbol{\theta}|\mathbf{y}) \propto \frac{\pi(\mathbf{y}|\mathbf{x}, \boldsymbol{\theta})\pi(\mathbf{x}|\boldsymbol{\theta})\pi(\boldsymbol{\theta})}{\pi(\mathbf{x}|\mathbf{y}, \boldsymbol{\theta})} \Big|_{\mathbf{x}=\boldsymbol{\mu}(\boldsymbol{\theta})} \quad (32)$$

3.4.1 Numerical optimization

What we have done so far, is to approximate the mean $\boldsymbol{\mu}(\boldsymbol{\theta})$ and selected entries of the variance $(\mathbf{Q}(\boldsymbol{\theta}))^{-1}$ under fixed hyperparameter configuration $\boldsymbol{\theta}$. However, if we want to find the mode of the marginal $\pi(\boldsymbol{\theta}|\mathbf{y})$, we have to use a gradient based optimization algorithm. The gradient ascent/descent and the Newton method are two common choices, and can be written using a single formula

$$\boldsymbol{\theta}^{(k+1)} = \boldsymbol{\theta}^{(k)} - \rho^{(k)} \cdot (\mathbf{H}^{(k)})^{-1} \nabla \log \pi(\boldsymbol{\theta}^{(k)}|\mathbf{y}). \quad (33)$$

where $\rho^{(k)}$ is a learning rate parameter. For general references, please see Amari [1993], Kiwiel [2001], Bottou [1998]. Choosing the preconditioner to be the negative identity $\mathbf{H}^{(k)} = -\mathbf{I}$ yields the gradient descent/ascent algorithm, the exact Hessian $\mathbf{H}^{(k)} = \nabla^2 \log \pi(\boldsymbol{\theta}^{(k)}|\mathbf{y})$ results in (damped) Newton method and an approximation to the Hessian gives us so-called quasi-Newton methods. When the gradient is randomized the algorithm is essentially a stochastic gradient descent or a stochastic Newton method. For the guaranteed convergence of the stochastic gradient descent, $\rho^{(k)}$ has to diminish with k and the stochastic gradient must have bounded variance. Also, the stochastic Newton can be unstable due to noise and is biased unless we have the exact full Hessian, which is not possible in our context. However, one could employ an approximate but deterministic preconditioner $\mathbf{H}^{(k)}$ that would still be better than uniform scaling of the gradient descent. We use a diagonal matrix of second derivatives, obtained from two first derivatives with stochastic components removed.

3.4.2 Gradient estimation

Next, we show how we can approximate the gradient using the RBMC estimator of the partial inverse. Three densities in the Equation (32) except $\pi(\boldsymbol{\theta})$ are Gaussian. Thus, it will involve computing the quantities $\frac{\partial}{\partial \theta_j} \log |\mathbf{Q}_y(\boldsymbol{\theta})|$,

$\frac{\partial}{\partial \theta_j} \log |\mathbf{Q}_x(\boldsymbol{\theta})|$, $\frac{\partial}{\partial \theta_j} \log |\mathbf{Q}(\boldsymbol{\theta})|$, as well as $\frac{\partial}{\partial \theta_j} (\mathbf{y} - \mathbf{Ax})^\top \mathbf{Q}_y(\boldsymbol{\theta}) (\mathbf{y} - \mathbf{Ax})$, $\frac{\partial}{\partial \theta_j} \mathbf{x}^\top \mathbf{Q}_x(\boldsymbol{\theta}) \mathbf{x}$, $\frac{\partial}{\partial \theta_j} (\mathbf{x} - \boldsymbol{\mu}(\boldsymbol{\theta}))^\top \mathbf{Q}(\boldsymbol{\theta}) (\mathbf{x} - \boldsymbol{\mu}(\boldsymbol{\theta}))$ for the partial derivatives. The quadratic forms can be computed directly using the finite differences, but the log-determinants are harder to approximate. We use the following fact

$$\begin{aligned} \frac{\partial}{\partial \theta_j} \log |\mathbf{Q}(\boldsymbol{\theta})| &= \frac{\partial}{\partial \theta_j} (\log |\mathbf{Q}_{uu}(\boldsymbol{\theta})| + \log |\mathbf{S}(\boldsymbol{\theta})|) \\ &= \text{tr}(\mathbf{Q}_{uu}(\boldsymbol{\theta})^{-1} \frac{\partial}{\partial \theta_j} \mathbf{Q}_{uu}(\boldsymbol{\theta})) \\ &\quad + \text{tr}(\mathbf{S}(\boldsymbol{\theta})^{-1} \frac{\partial}{\partial \theta_j} \mathbf{S}(\boldsymbol{\theta})) \end{aligned} \quad (34)$$

where $\mathbf{S}(\boldsymbol{\theta})$ is the Schur complement of $\mathbf{Q}_{uu}(\boldsymbol{\theta})$ in $\mathbf{Q}(\boldsymbol{\theta})$. The trace of the latter can be computed using dense linear algebra, since the dimensions of the matrix ($n_\beta \times n_\beta$) are assumed to be small. On the other hand, the first term can be expressed as sum over the elementwise product of the inverse and the partial derivative, meaning that we have to know the inverse $\mathbf{Q}_{uu}(\boldsymbol{\theta})^{-1}$ only at nonzero positions of $\frac{\partial}{\partial \theta_j} \mathbf{Q}_{uu}(\boldsymbol{\theta})$ or $\mathbf{Q}_{uu}(\boldsymbol{\theta})$, i.e. the selected inverse. We can compute the trace in parallel, because the precision matrix, its inverse and derivatives are already distributed along corresponding rows Ω_p .

$$\begin{aligned} \text{tr}(\mathbf{Q}_{uu}(\boldsymbol{\theta})^{-1} \frac{\partial}{\partial \theta_j} \mathbf{Q}_{uu}(\boldsymbol{\theta})) &= \\ &= \sum_{i,k} \left[\mathbf{Q}_{uu}(\boldsymbol{\theta})^{-1} \odot \frac{\partial}{\partial \theta_j} \mathbf{Q}_{uu}(\boldsymbol{\theta}) \right]_{ik} \\ &= \sum_{p=1}^{n_p} \sum_{i,k} \left[\left(\mathbf{Q}_{uu}(\boldsymbol{\theta})^{-1} \right)_{\Omega_p \Omega_p^*} \odot \left(\frac{\partial}{\partial \theta_j} \mathbf{Q}_{uu}(\boldsymbol{\theta}) \right)_{\Omega_p \Omega_p^*} \right]_{ik} \end{aligned} \quad (35)$$

Therefore, we can use our selected inversion method in Algorithm 3.3 to compute partial derivatives of $\log |\mathbf{Q}(\boldsymbol{\theta})|$ and $\log |\mathbf{Q}_x(\boldsymbol{\theta})|$, and hence, of $\log \pi(\boldsymbol{\theta}|\mathbf{y})$. Please find the rough algorithm below (trivial partial derivatives are omitted) in Algorithm 3.6.

Algorithm 3.6 Hyperparameter estimation

Input: $\boldsymbol{\theta}^{(0)}$

```

for  $k = 1, \dots$ , convergence do
  Solve for  $\boldsymbol{\mu}(\boldsymbol{\theta})$  and  $\mathbf{S}(\boldsymbol{\theta})$ 
   $\mathbf{Q}(\boldsymbol{\theta})^{-1} \approx \text{RBMC}(\mathbf{Q}(\boldsymbol{\theta}))$ 
   $\mathbf{Q}_x(\boldsymbol{\theta})^{-1} \approx \text{RBMC}(\mathbf{Q}_x(\boldsymbol{\theta}))$ 
  for  $j = 1, \dots, n_\theta$  do
    Compute  $\frac{\partial}{\partial \theta_j} \log |\mathbf{Q}(\boldsymbol{\theta})|$ ,  $\frac{\partial}{\partial \theta_j} \log |\mathbf{Q}_x(\boldsymbol{\theta})|$ 
    and other terms in the derivative
    Compute  $\frac{\partial}{\partial \theta_j} \log \pi(\boldsymbol{\theta}|\mathbf{y})$ 
  end for
  Update  $\rho^{(k)}$ ,  $\mathbf{H}^{(k)}$ 
   $\boldsymbol{\theta}^{(k+1)} = \boldsymbol{\theta}^{(k)} - \rho^{(k)} \cdot (\mathbf{H}^{(k)})^{-1} \nabla \log \pi(\boldsymbol{\theta}^{(k)}|\mathbf{y})$ 
end for
Return  $\boldsymbol{\theta}^{(k)}$ 

```

Output: $\text{diag}(\boldsymbol{\Sigma})$

4 Numerical results

In this section, we will apply the methods described in Section 3 on a simulated data and a real world example. For demonstration purposes, we will consider thin 3D models with small temporal separators, usually found in applications for daily weather data. We will model the spatio-temporal component in both examples by a critical diffusion model

with parameters $(\alpha_t, \alpha_s, \alpha) = (1, 2, 1)$ [Lindgren et al., 2020]. In the following examples, we consider both the fixed and unknown hyperparameters cases, in latter setting, we impose the PC prior on θ .

$$\begin{aligned} \mathbf{y}|\mathbf{x}, \theta &\sim \mathcal{N}(\mathbf{A}\mathbf{x}, \mathbf{Q}_y^{-1}) \\ \mathbf{x}|\theta &\sim \mathcal{N}(\mathbf{0}, \mathbf{Q}_x^{-1}) \\ \theta &\sim \pi_{\text{PC}}(\theta) \end{aligned} \quad (36)$$

The full conditional read as

$$\mathbf{x}|\mathbf{y}, \theta \sim \mathcal{N}(\boldsymbol{\mu}, \mathbf{Q}^{-1}), \quad (37)$$

where $\mathbf{Q} = \mathbf{Q}_x + \mathbf{A}^T \mathbf{Q}_y \mathbf{A}$ and $\boldsymbol{\mu} = \mathbf{Q}^{-1} \mathbf{A}^T \mathbf{Q}_y \mathbf{y}$ depend on θ . The posterior mean and marginal variances are computed according to the Equation (20) and Algorithms 3.4 and 3.5. The implementation of the algorithms was written in C using the PETSc library [Balay et al., 1997] and MUMPS as the direct solver [Amestoy et al., 2001]. While PARDISO Schenk et al. [2001] is superior, we use MUMPS because it is free and open source.

It is important to note that the posterior precision matrix is not assembled explicitly, only the first block \mathbf{Q}_{uu} corresponding to the spatio-temporal field. This is done to ease the implementation and reduce the load imbalance. The spatio-temporal block itself is computed from the sum of Kronecker products of temporal \mathbf{J} and spatial \mathbf{K} matrices. The mesh and the matrices can be generated by the R-INLA package in R language.

For space-time models that are long in time direction, the partitioning naturally divides the graph into time intervals. In this case, some simplifications can be done to assemble the precision matrices. For instance, if we distribute the rows of temporal \mathbf{J} matrices to different processes, Kronecker products $\mathbf{J} \otimes \mathbf{K}$ can be computed locally as long as \mathbf{K} is available at each process. This helps to efficiently assemble the matrix in parallel without computing the full Kronecker product. The same goes for a projection matrix \mathbf{A}_u , which can be expressed as a Kronecker product between temporal and spatial projections $\mathbf{A}_t \otimes \mathbf{A}_s$.

4.1 Simulated example

Now we present some results for a simulated example, where we generate a synthetic data and fit a space-time model. The observations are generated as $y(\mathbf{s}, t) = 1 + t + \sin(6\pi t) + \epsilon$, with 1 and t being the covariates and $\epsilon \sim \mathcal{N}(0, 1.01)$. The locations \mathbf{s} are sampled uniformly on a sphere. The mesh consists of $n_s = 162$ nodes on a sphere and $n_t = 100$ nodes in time, $n_u = 16,200$ in total. First, we assume that hyperparameters are fixed to: $r_s = 1$, $r_t = 10$, $\sigma^2 = 1$, $\tau_y = \exp(1)$. We divide the field into 4 temporal partitions Ω_p , which are then extended to overlapping Ω_p^* using $n_l = 1$ neighbors. Each partition owns all 162 nodes in space, 25 non-overlapping nodes in time and 26-27 with the overlap, totaling at least 8,262 nodes per process. The number of samples for the RBMC estimator is $n_k = 5$. We compute the posterior marginals for fixed hyperparameters using R-INLA package and our own approximation from Section 3. The posterior marginal mean and standard deviation for the field at time $t = 25$ (on the boundary of the partition) are visualized in Figure 5.

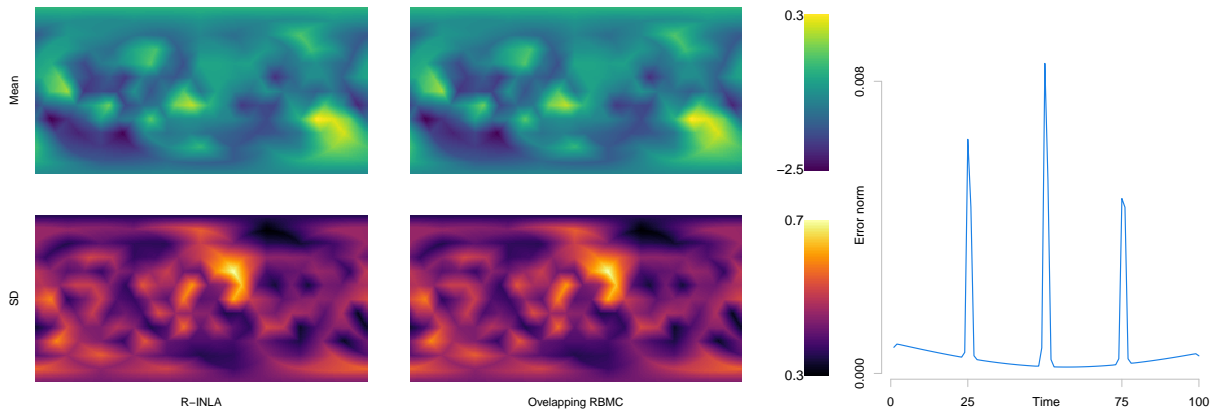


Figure 5: Left: Posterior mean (first row) and standard deviation (second row) at $t = 25$ using R-INLA (3.94 sec/fn-call) and Overlapping RBMC (1.47 sec/fn-call). Right: The relative error of overlapping RMBC estimator for the posterior marginal variance versus time.

As we see, the posterior plots are almost indistinguishable. This is expected due to good conditioning of the precision matrix, despite the slice being near the separating set at $t = 26$. To see the overall behavior of the RBMC estimator,

let us fix the spatial location and plot the error against time. The maximum relative error of marginal variance for a single spatial node is given on the right in Figure 5. We clearly see how error rises, as we approach the boundaries of a partition, behaving as described in Section 3. However, the approximation is also very precise near the separator, and the maximum relative error does not exceed 10^{-2} . Setting the overlap parameter to be equal to the temporal range $n_l = r_t = 10$ would give the error of the magnitude 10^{-12} . At this distance, the correlation drops to negligible levels and almost no correction is needed from sampling. Of course, one could decrease n_l and increase the number of samples K , and still achieve the same level of accuracy. In the end, the parameter choice will depend on not only the temporal range, but also on other hyperparameters, as well as the problem size and hardware constraints.

Now, we relax our assumptions and treat the hyperparameters as unknowns. We optimize for the hyperparameters using Algorithm 3.6 and our approximation to the gradient. As a reference, we first run the R-INLA package, which produces $\theta_{\text{INLA}}^* = (-1.141, 0.503, 0.340, 4.580)$ in 158.2 seconds with 0.347 seconds per function call. In comparison, our optimizer converges to $\theta_{\text{RBMC}}^* = (-1.144, 0.501, 0.341, 4.575)$ in 15 iterations and 286.7 seconds (about 1.713 seconds per function call), with relative norm of the gradient $< 10^{-3}$ and $\|\theta_{\text{RBMC}}^* - \theta_{\text{INLA}}^*\| = 0.00579$. We used a “warm” start $\theta_{\text{RBMC}}^{(0)} = (-1, 0, 0, 3)$, a learning rate $\rho = 0.9$, a diagonal Hessian approximation from the deterministic part of the RBMC estimator. R-INLA is a highly optimized library and our code is slower for this problem, but it requires much less storage (peak 43 MB opposed to 4.6 GB) and is able to run in a distributed setting.

4.1.1 Strong and weak scaling

We now also present running times for the same simulation problem with different number of processes and temporal dimensions. All runs were conducted on Intel nodes of the Ibex cluster at KAUST. The Table 1 shows results for a fixed problem size, with $n_s = 162$ and $n_t = 1,658,880$, but differing number of processors (partitions). In an ideal situation, the inference time decreases twice every time we double the number of processors. We see that this is not entirely the case, and with 1024 processors (on 67 nodes) we even start to see an increase. At this point, the communication costs start to outweigh the benefits of parallelization.

Table 1: Running time for fixed problem size (1,658,880 unknowns)

	10240	10240	10240	10240	10240	10240	10240	10240	10240	10240
n_t	10240	10240	10240	10240	10240	10240	10240	10240	10240	10240
n_p	2	4	8	16	32	64	128	256	512	1024
times (s)	588.62	331.84	194.09	89.06	51.12	29.53	19.73	13.40	11.16	13.30

What we are also interested in is how well the inference scales with fixed problem size per process. In this case, we can measure the overhead and inefficiencies in communication. The Table 2 summarizes the times for various number of processes (partitions). The spatial dimensions of the problem are the same, $n_s = 162$. The temporal dimensions per process are fixed to $n_t/n_p = 100$, and to $n_t/n_p + 2n_l = 120$ with the overlap, totalling 19,440 unknowns per process. In total, we have 16,588,800 unknown variables. We see that the running time slowly increases, doubling for 128 cores (26 nodes) and quadrupling for 1024 cores (75 nodes). The corresponding plot in Figure 6 shows this steady decrease in efficiency.

Table 2: Running time for fixed workload per process (19,440 unknowns)

	200	400	800	1600	3200	6400	12800	25600	51200	102400
n_t	200	400	800	1600	3200	6400	12800	25600	51200	102400
n_p	2	4	8	16	32	64	128	256	512	1024
times (s)	11.71	12.42	13.50	15.53	19.74	20.83	24.56	31.97	35.34	49.10

4.2 Application to US daily temperature data

We conclude the section by demonstrating the results obtained using our method for the US temperature data [Menne et al., 2012]. The data consists of 12 years (4383 days) of daily temperature observations, recorded at 4730 stations across the continental US. Apart from the time and location information, we are also provided with elevation. We additionally include the y-coordinates and the first harmonics (sine and cosine) as the covariates for seasonal temperature variation. In total, there are 5 covariates including the intercept. The spatio-temporal field is modeled using the critical diffusion (121) model. First, we fit a subset of the original dataset using INLA and our method. The hyperparameters are estimated on a 1-year dataset using 100 stations and mesh sizes $n_s = 119$ and $n_t = 365$. The hyperparameter vector estimated by R-INLA is $\theta_{\text{INLA}}^* = (7.850, 4.529, 2.050, -2.039)$, that is, $r_s = 2566.4$, $r_t = 92.65$, $\sigma^2 = 7.768$

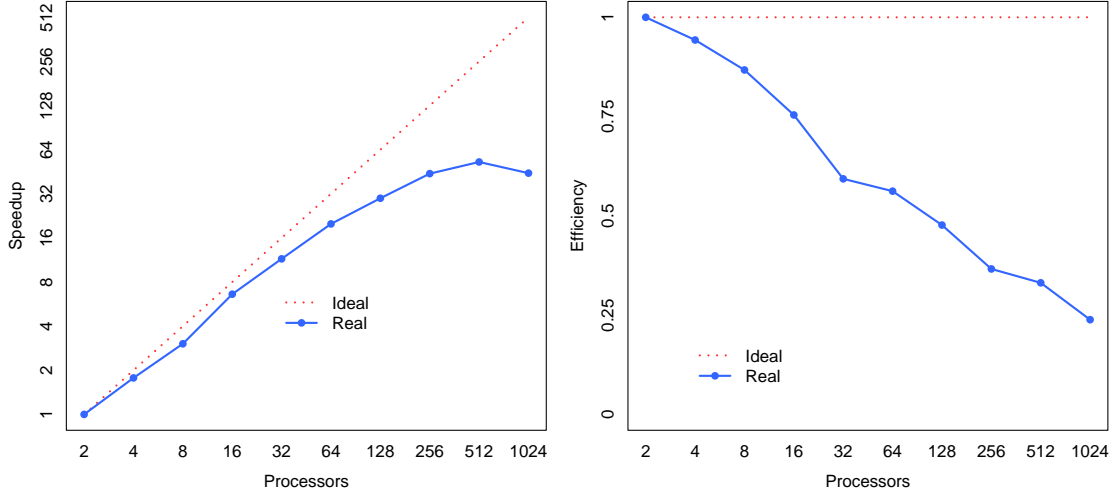


Figure 6: Strong and weak scaling for inference based on overlapping RBMC algorithm

and $\tau_y = 0.130$. The corresponding RBMC estimate is $\theta_{\text{RBMC}}^* = (7.043, 2.867, 1.627, -1.999)$, which is $r_s = 1144.8$, $r_t = 17.58$, $\sigma^2 = 5.088$ and $\tau_y = 0.135$. We used $\rho = 0.5$, $n_k = 20$, a diagonal Hessian and “warm” starting values $\theta_{\text{RBMC}}^{(0)} = (7, 0, 0, 0)$. Larger models could not be run using R-INLA on a computer with only 16 GB of RAM. It took R-INLA 288.9 seconds with peak memory usage of 7.81 GB on 12 threads. On the other hand, our implementation required only 108.7 MB of memory, but it ran for about 1070.3 seconds using 6 cores (6 threads). The run time difference can be due to R-INLA using a deterministic Newton method with line search and being less wasteful, whereas our approach is stochastic and typically needs longer runs. We also note that the gradient norm of the objective function did not change dramatically in the vicinities of θ_{INLA}^* and θ_{RBMC}^* , meaning that if we use the gradient norm as a stopping criterion, we might end up in different parts of the target when starting from different initial positions. E.g. we obtain $\theta_{\text{RBMC}}^* \approx (5, 3, 2 - 2)$ when starting from $(0, 0, 0, 0)$. This might explain the discrepancy in θ estimates.

Now we do the inference on the full dataset using the spatial and temporal mesh generated by R-INLA, which have respective dimensions $n_s = 926$ and $n_t = 4383$. The total size of the spatio-temporal field is therefore $n = 4,058,658$. Once more, the graph can be easily partitioned along the temporal axis. The overlap parameter is $n_l = 1$, the number of partitions (processes) is $n_p = 100$. Each process gets about 22 non-overlapping time points and about 24 with the overlap. Then the median workload per process is $24 \times 926 = 20,372$. We set the number of samples to $n_k = 10$. The code took 4744.05 seconds to run on 100 cores on multiple nodes of KAUST’s Ibex cluster. We use the learning rate of $\rho^{(k)} = 0.8^{k \bmod 10}$, $n_k = 10$, a diagonal Hessian and “cold” initial values $\theta_{\text{RBMC}}^{(0)} = (0, 0, 0, 0)$. The code run until the relative norm of the gradient reached 10^{-3} . The estimated hyperparameter values are $\theta_{\text{RBMC}}^* = (4.492, 0.978, 3.080, -2.324)$.

Below we plot posterior marginals for several slices of the spatio-temporal field at $t \in \{21, 22, 365, 4383\}$, where $t = 22$ corresponds to the boundary of the first partition. The posterior mean seems to capture the effects of geographical features on the temperature well. For instance, the western part of the US remains the same throughout both 2-day windows in January and July. At the same time, the central part experiences more rapid changes. The January (left) plots shows the cold front (dark) moving eastwards. The second row shows the posterior marginal standard deviations. The overall picture is not as dynamic, but we can see that the uncertainty is lower in regions with more observations. The variance increases outside of the boundaries, which is very typical for the SPDE approach.

5 Conclusion

In this paper, we have presented a scalable distributed approach for approximating the posterior marginals of spatio-temporal GMRFs and approximating the hyperparameters. The proposed methods rely on Krylov solvers for computing the posterior mean and sampling, and a hybrid Rao-Blackwellized Monte Carlo approach for estimating the posterior marginal variances. We then reuse the obtained partial inverse to construct a stochastic gradient direction during the optimization step. The major emphasis was put on the scalability of algorithms in a setting, where the matrices are prohibitively large and are distributed among many cluster nodes. The numerical results demonstrated that the

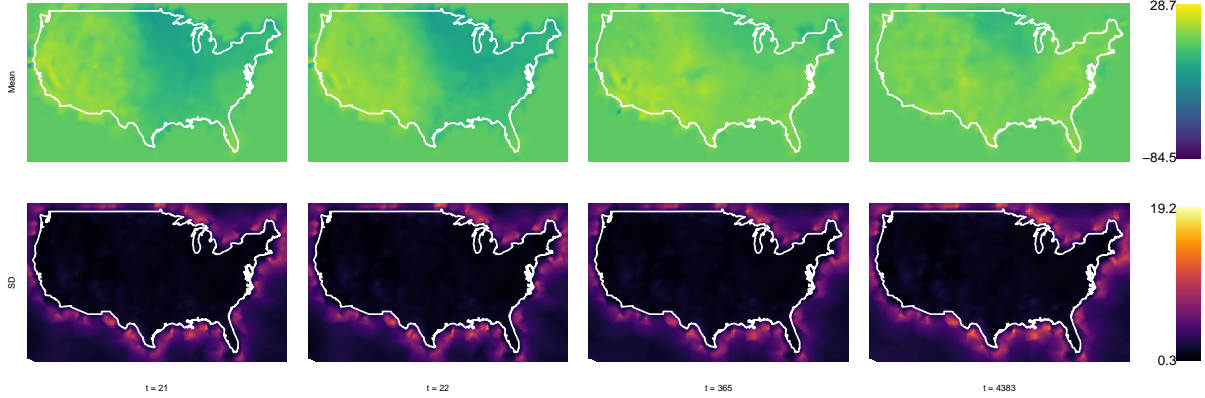


Figure 7: Posterior mean (first row) and standard deviation (second row) at $t \in \{21, 22, 365, 4383\}$ from the overlapping RBMC estimator.

approximation can recover the posterior parameters from R-INLA and the implementation can scale on up to 1024 cores on 76 nodes.

Profiling our code also showed that the main computational bottlenecks are direct factorization and sampling. Thus, future optimizations to reduce the total run time may include a more efficient extension of partitions and a more localized strategy for generating samples. For instance, the overlap parameter could be computed dynamically by using probing techniques to approximate the posterior correlation range. Then we can generate more compact overlaps and waste less resources on uncorrelated halo regions. To reduce the communication time during sampling stage, one could try to form samples from the separators directly, rather than solving for global samples. Lastly, we also note that the condition of the precision matrix \mathbf{Q} is highly dependent on the hyperparameter configuration, which affects overall convergence of Krylov methods, correlation of the field components, and hence the efficiency of any method based on partitioning the graph.

The results can be extended in three main ways. First, the proposed methods considers only Gaussian distributed observations, for which we have closed form posterior densities. Other likelihoods could be added by iterating the Gaussian approximation several times, which corresponds to applying a Newton-Raphson method for non-linear problems. Computationally, this only adds a few more linear solves during iterations. Second, the hyperparameters of the field and the likelihood are approximated only at the mode in our examples. To compute the full posterior distribution of hyperparameters, one can employ a numerical integration scheme as in the INLA methodology [Rue et al., 2009, 2017]. Then one has to compute the full Hessian of the log-density $\log \pi(\boldsymbol{\theta}|\mathbf{y})$ to place the integration points around the mode. Finally, the mesh and the arguments n_l, n_k of the inversion algorithm can be set dynamically every time when hyperparameter values change during optimization. However, this will most likely result in different workload for different values of $\boldsymbol{\theta}$ and requires one to re-generate and re-distribute the mesh at each iteration.

To sum up, the proposed method provides a scalable way to perform a Bayesian inference on large spatio-temporal GMRFs. Our approach is particularly well suited for daily weather applications, where thin 3D graphs produce compact separators in time. The source code with examples can be found on Github <https://github.com/abylayzhumekenov/parsinv>.

References

- Finn Lindgren, Håvard Rue, and Johan Lindström. An explicit link between gaussian fields and gaussian markov random fields: the stochastic partial differential equation approach. *Journal of the Royal Statistical Society Series B: Statistical Methodology*, 73(4):423–498, 2011.
- Finn Lindgren, David Bolin, and Håvard Rue. The spde approach for gaussian and non-gaussian fields: 10 years and still running. *Spatial Statistics*, 50:100599, 2022.
- Håvard Rue, Sara Martino, and Nicolas Chopin. Approximate bayesian inference for latent gaussian models by using integrated nested laplace approximations. *Journal of the Royal Statistical Society Series B: Statistical Methodology*, 71(2):319–392, 2009.
- Håvard Rue, Andrea Riebler, Sigrunn H Sørbye, Janine B Illian, Daniel P Simpson, and Finn K Lindgren. Bayesian computing with inla: a review. *Annual Review of Statistics and Its Application*, 4:395–421, 2017.

- Esmail Abdul Fattah and Haavard Rue. Approximate bayesian inference for the interaction types 1, 2, 3 and 4 with application in disease mapping. *arXiv preprint arXiv:2206.09287*, 2022.
- Lisa Gaedke-Merzhäuser, Janet van Niekerk, Olaf Schenk, and Håvard Rue. Parallelized integrated nested laplace approximations for fast bayesian inference. *Statistics and Computing*, 33(1):25, 2023.
- Lisa Gaedke-Merzhäuser, Elias Krainski, Radim Janalik, Håvard Rue, and Olaf Schenk. Integrated nested laplace approximations for large-scale spatiotemporal bayesian modeling. *SIAM Journal on Scientific Computing*, 46(4): B448–B473, 2024.
- AM Erisman and WF Tinney. On computing certain elements of the inverse of a sparse matrix. *Communications of the ACM*, 18(3):177–179, 1975.
- Joseph WH Liu. Computational models and task scheduling for parallel sparse cholesky factorization. *Parallel computing*, 3(4):327–342, 1986.
- Xiaoye S Li and James W Demmel. Superlu_dist: A scalable distributed-memory sparse direct solver for unsymmetric linear systems. *ACM Transactions on Mathematical Software (TOMS)*, 29(2):110–140, 2003.
- Yousef Saad. *Iterative methods for sparse linear systems*. SIAM, 2003.
- Michael K Schneider and Alan S Willsky. A krylov subspace method for covariance approximation and simulation of random processes and fields. *Multidimensional systems and signal processing*, 14:295–318, 2003.
- Daniel P Simpson, Ian W Turner, and Anthony N Pettitt. Fast sampling from a gaussian markov random field using krylov subspace approaches. 2008.
- George Papandreou and Alan L Yuille. Gaussian sampling by local perturbations. *Advances in Neural Information Processing Systems*, 23, 2010.
- Albert Parker and Colin Fox. Sampling gaussian distributions in krylov spaces with conjugate gradients. *SIAM Journal on Scientific Computing*, 34(3):B312–B334, 2012.
- Daniel P Simpson, Ian W Turner, Christopher M Strickland, and Anthony N Pettitt. Scalable iterative methods for sampling from massive gaussian random vectors. *arXiv preprint arXiv:1312.1476*, 2013.
- Edmond Chow and Yousef Saad. Preconditioned krylov subspace methods for sampling multivariate gaussian distributions. *SIAM Journal on Scientific Computing*, 36(2):A588–A608, 2014.
- Michael F Hutchinson. A stochastic estimator of the trace of the influence matrix for laplacian smoothing splines. *Communications in Statistics-Simulation and Computation*, 18(3):1059–1076, 1989.
- Jok M Tang and Yousef Saad. A probing method for computing the diagonal of a matrix inverse. *Numerical Linear Algebra with Applications*, 19(3):485–501, 2012.
- Per Sidén, Finn Lindgren, David Bolin, and Mattias Villani. Efficient covariance approximations for large sparse precision matrices. *Journal of Computational and Graphical Statistics*, 27(4):898–909, 2018.
- Finn Lindgren, Haakon Bakka, David Bolin, Elias Krainski, and Håvard Rue. A diffusion-based spatio-temporal extension of gaussian markov random fields. *arXiv preprint arXiv:2006.04917*, 2020.
- Peter Whittle. On stationary processes in the plane. *Biometrika*, pages 434–449, 1954.
- Peters Whittle. Stochastic-processes in several dimensions. *Bulletin of the International Statistical Institute*, 40(2): 974–994, 1963.
- Chuan Miao Chen and Vidar Thomée. The lumped mass finite element method for a parabolic problem. *The ANZIAM Journal*, 26(3):329–354, 1985.
- Finn Lindgren and Håvard Rue. Bayesian spatial modelling with r-inla. *Journal of statistical software*, 63(19), 2015.
- David Bolin and Kristin Kirchner. The rational spde approach for gaussian random fields with general smoothness. *Journal of Computational and Graphical Statistics*, 29(2):274–285, 2020.
- Janet Van Niekerk, Elias Krainski, Denis Rustand, and Håvard Rue. A new avenue for bayesian inference with inla. *Computational Statistics & Data Analysis*, 181:107692, 2023.
- Havard Rue and Leonhard Held. *Gaussian Markov random fields: theory and applications*. Chapman and Hall/CRC, 2005.
- Fabio Verbosio, Arne De Coninck, Drosos Kourounis, and Olaf Schenk. Enhancing the scalability of selected inversion factorization algorithms in genomic prediction. *Journal of computational science*, 22:99–108, 2017.
- Gene H Golub and Gérard Meurant. Matrices, moments and quadrature. *Pitman Research Notes in Mathematics Series*, pages 105–105, 1994.

- Shashanka Ubaru, Jie Chen, and Yousef Saad. Fast estimation of $\text{tr}(f(a))$ via stochastic lanczos quadrature. *SIAM Journal on Matrix Analysis and Applications*, 38(4):1075–1099, 2017.
- Andreas Frommer, Claudia Schimmel, and Marcel Schweitzer. Analysis of probing techniques for sparse approximation and trace estimation of decaying matrix functions. *SIAM Journal on Matrix Analysis and Applications*, 42(3):1290–1318, 2021.
- Daniel Simpson, Håvard Rue, Andrea Riebler, Thiago G Martins, and Sigrunn H Sørbye. Penalising model component complexity: A principled, practical approach to constructing priors. 2017.
- Shun-ichi Amari. Backpropagation and stochastic gradient descent method. *Neurocomputing*, 5(4-5):185–196, 1993.
- Krzysztof C Kiwiel. Convergence and efficiency of subgradient methods for quasiconvex minimization. *Mathematical programming*, 90:1–25, 2001.
- Léon Bottou. Online algorithms and stochastic approximations. *Online learning in neural networks*, 1998.
- Satish Balay, William D. Gropp, Lois Curfman McInnes, and Barry F. Smith. Efficient management of parallelism in object oriented numerical software libraries. In E. Arge, A. M. Bruaset, and H. P. Langtangen, editors, *Modern Software Tools in Scientific Computing*, pages 163–202. Birkhäuser Press, 1997.
- Patrick R Amestoy, Iain S Duff, Jean-Yves L’Excellent, and Jacko Koster. A fully asynchronous multifrontal solver using distributed dynamic scheduling. *SIAM Journal on Matrix Analysis and Applications*, 23(1):15–41, 2001.
- Olaf Schenk, Klaus Gärtner, Wolfgang Fichtner, and Andreas Stricker. Pardiso: a high-performance serial and parallel sparse linear solver in semiconductor device simulation. *Future Generation Computer Systems*, 18(1):69–78, 2001.
- Matthew J Menne, Imke Durre, Russell S Vose, Byron E Gleason, and Tamara G Houston. An overview of the global historical climatology network-daily database. *Journal of atmospheric and oceanic technology*, 29(7):897–910, 2012.